Ultra-low-power saturation of an ISB transition by a mid-IR quantum cascade laser

M. Jeannin,[1, a)] E. Cosentino,[1] S. Pirotta,[1] M. Malerba,[1] G. Biasiol,[2] J.-M. Manceau,[1] and R. Colombelli[1]
[1)] *Centre de Nanosciences et de Nanotechnologies, CNRS UMR 9001, Université Paris Saclay, 10 Boulevard Thomas Gobert, 91120 Palaiseau*
[2)] *Laboratorio TASC, CNR-IOM, Area Science Park, S.S. 14 km 163.5, Basovizza I-34149 Trieste, Italy*

(Dated: 22 December 2022)

We demonstrate that absorption saturation of a mid-infrared intersubband transition can be engineered to occur at moderate light intensities of the order of 10-20 kW.cm^{-2} and at room temperature. The structure consists of an array of metal-semiconductor-metal patches hosting a judiciously designed 253 nm thick GaAs/AlGaAs semiconductor heterostructure. At low incident intensity the structure operates in the strong light-matter coupling regime and exhibits two absorption peaks at wavelengths close to 8.9 μm. Saturation is detected as a transition to the weak coupling regime - and therefore to a single-peaked absorption - when increasing the incident power. Comparison with a coupled mode theory model explains the data and permits to infer the relevant system parameters. At selected wavelengths the reflectivity non-linearly increases with increasing incident power. This system can therefore be engineered to implement saturable absorption mirrors (SESAMs) in the mid-IR range, a technology currently missing.

Semiconductor saturable absorber mirrors (SESAMs) are semiconductor mirrors with a reflectivity that increases non-linearly with the incident optical power. They rely on the absorption saturation of an interband transition in a thin absorbing semiconductor layer on top of a Bragg mirror, and have been crucial devices in the emergence of passively mode-locked solid-state lasers operating at visible and near-infrared frequencies[1–3]. They enabled the development of ultra-short pulses sources and frequency combs that became relatively *easily* available in those wavelength ranges. Their extension to the mid-infrared (mid-IR) region ($\lambda \approx 3-12$ µm) would represent a great step for ultrafast mid-IR lasers. As the mid-IR hosts characteristic molecular vibrational modes, it is an extremely important spectral range for fundamental science like metrology and spectroscopy, as well as numerous applications in environmental monitoring and space science, to name a few. Unfortunately, conventional SESAMs cannot extend directly to the mid-IR because the photon energy is smaller than the gap of most common semiconductor materials. Recent efforts have thus been directed to find new suitable material systems, relying e.g. on type II superlattices[4] or two dimensional materials like graphene[5] and transition metal dichalcogenides[6] (see e.g. Ref.[7] for a recent review). However, the complexity of designing type II superlattice SESAM at longer wavelength along with the challenges posed by increasingly thicker Bragg mirror layers hinders their development, while obtaining large area of good quality two dimensional materials poses a strong limit on the scalability of this method.

As an alternative to interband transitions, intersubband (ISB) transitions between confined energy levels of doped semiconductor quantum wells (QWs) are tunable accross the entire mid-IR range. Their most popular realization is the development of practical mid-IR semiconductor lasers[8] with the invention of the quantum cascade laser[9]. Since then, ISB transitions have contributed to the extension of semiconductor optoelectronic devices to the mid-IR and THz ranges of the electromagnetic spectrum. Examples are the demonstration and commercialization of mid-IR photodetectors[10–14], free-space amplitude modulators[15,16], and the enhancement of parametric frequency conversion schemes, resulting in efficient cavity-enhanced second and third harmonic generation[17–21]. Unfortunately, the very short non-radiative lifetime of ISB transitions ($\approx ps$) leads to high saturation intensities[22–25], in the MW.cm^{-2} range. These high values are *in principle* not compatible with conventional semiconductor lasers output powers, which has prevented up to now the development of ISB-based SESAMs.

In this work, we experimentally demonstrate that the absorption saturation of mid-IR intersubband transitions can be drastically reduced down to the kW.cm^{-2} range. Such low values are compatible with the output power of commercially available quantum cascade lasers (QCL), interband cascade lasers (ICL) and emerging mid-IR fiber lasers[26,27]. As detailed in our recent theoretical work[28], this requires embedding a judiciously designed semiconductor active region in metallic microcavities to operate the system at the onset of the strong light-matter coupling regime. In this regime, the response of the coupled ISB transition - cavity mode takes the form of two coupled light-matter states called *polaritons*. These polaritons are split in frequency by twice the vacuum Rabi frequency Ω_R, which quantifies the strength of the light-matter interaction and is directly expressed as:

$$\Omega_R^2 = f_w f_{12} \frac{\Delta n\ e^2}{4\varepsilon\varepsilon_0 m^* L_{qw}} = a\Delta n \qquad (1)$$

[a)] mathieu.jeannin@universite-paris-saclay.fr

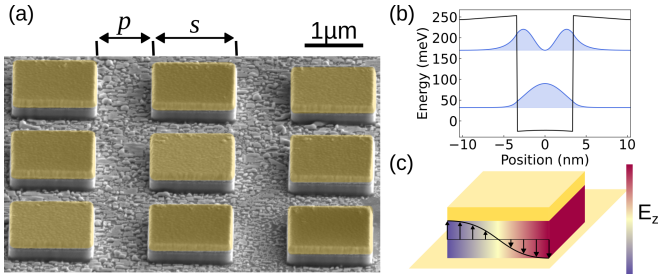

FIG. 1. (a) Colorized bird's eye view SEM image of a typical patch antenna array defining the relevant dimensions s and p. (b) Self-consistent Schrödinger-Poisson simulation of a period of the structure showing the two confined electronic states. (c) Sketch of a single patch antenna with the electric field amplitude of the fundamental TM_{00} mode.

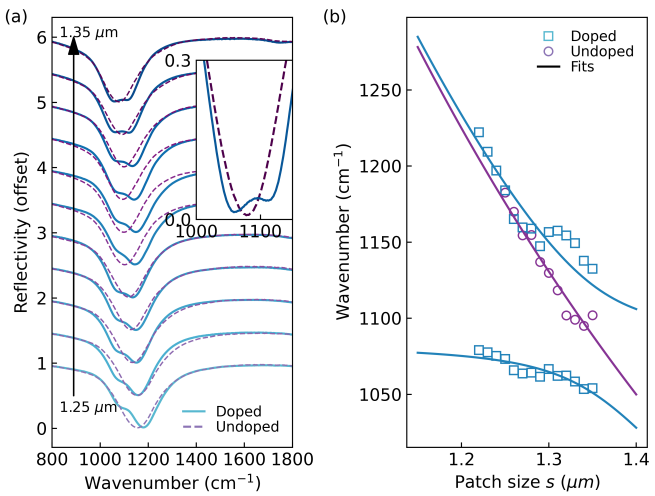

FIG. 2. (a) Reflectivity of the bare cavity arrays (purple dashed line) and of the doped cavity arrays (blue solid lines) as a function of the cavity size from $s = 1.24$ µm (bottom spectrum) to $s = 1.35$ µm (top spectrum). The spectra are offset by 0.5 for clarity. The inset shows a zoom on the $s = 1.35$ µm spectrum around the polariton splitting. We normalize all the data by the reflectivity spectrum of a smooth gold surface. (b) Dispersion relation of the microcavity polaritons as a function of the patch size. The symbols are the experimental data (circles: undoped cavities, squares: doped cavities) extracted from single and bi-Lorentzian fits of the spectra. The solid lines are fit to the cavity dispersion relation (3) and to the polariton dispersion relation (4).

where f_w is the filling fraction of the QWs inside the active region, f_{12} is the transition oscillator strength hereafter approximated to the infinite square QW limit ($f_{12} = 0.96$), e and m^* are the electron charge and effective mass, ε_0 and ε are the vacuum permittivity and the semiconductor relative permittivity, L_{qw} is the QW width, and $\Delta n = n_1 - n_2$ is the population difference between the first (n_1) and the second (n_2) electronic levels of the QW. The absorption saturation manifests itself with the collapse of the light-matter coupling as both Δn, and thus Ω_R, tend to zero.

To achieve saturation with a low incident intensity, a careful balance has to be found. We recall here the main findings of Ref.[28]. The saturation intensity I_{sat} is defined as the intensity for which the population difference Δn is reduced to half the value of the introduced doping n_s, or - equivalently - the population in the excited level is $n_s/4$:

$$\Delta n_{I_{sat}} = \frac{n_s}{2} \iff n_{2,sat} = \frac{n_s}{4}. \qquad (2)$$

Structures with low doping densities, when introduced in a properly designed cavity, can exhibit low saturation intensities. However, if the doping is too small so that the polariton splitting cannot be resolved, the spectral signature of the saturation that is the collapse of the polariton splitting is masked by the cavity absorption. Increasing the doping allows to increase the frequency splitting, but leads to a linear increase in saturation intensity as $I_{sat} \propto \Omega_R^2$. One has to operate at the onset of the strong light-matter coupling regime, where a moderate Ω_R allows to spectrally resolve the polariton states while retaining a low I_{sat}.

We have designed a saturable absorber active region composed of seven repetitions of $GaAs/Al_{0.33}Ga_{0.67}As$ QWs (6.5/14 nm, total thickness 253 nm) delta-doped with Si atoms (HM4448) with surface density of 2 10^{11} cm^{-2}. Additional doping layers on each side of the multi-QW structure are introduced to compensate for Fermi level pinning at the semiconductor-metal interfaces. A reference sample (HM4445) with the same, but undoped, active region is also fabricated and studied to measure the bare cavity response. The active region is processed using standard Au-Au thermo-compressive wafer bonding (following the procedure in Ref.[29]), selective substrate removal in citric acid and electron beam lithography to fabricate arrays of metal-metal patch cavities as shown in Fig. 1(a). The semiconductor between adjacent Au patches is removed by a $SiCl_4$-based inductively coupled plasma reactive ion etching. A self-consistent Schrödinger-Poisson simulation (Fig. 1(b)) shows the conduction band profile and confined electronic states of the QWs, with an energy separation of 138 meV corresponding to a transition wavenumber of 1110 cm^{-1} or a wavelength of 9 µm. The patch cavity size s ranges from 1.25 µm to 1.35 µm to tune the frequency of the fundamental TM_{00} (Fig. 1(c)) mode across the ISB transition. The distance p between adjacent cavities is fixed at $p = 1$ µm to operate close to the critical coupling condition, ensuring maximal energy funneling in the system.

The samples are initially characterized in a Fourier-transform infrared (FTIR) spectrometer equipped with a Cassegrain microscope objective, to measure the reflectivity spectrum of each patch cavity array. The results are shown in Fig. 2(a) for both the undoped QWs sample (purple dashed lines) and the doped QWs sample (blue solid line). The undoped sample exhibits a single absorption dip, corresponding to dissipation due to ohmic losses

in the cavity. The absorption frequency ω_c decreases with increasing patch size s following the usual relation:

$$\omega_c = \frac{\pi c}{n_{eff} s} \tag{3}$$

where n_{eff} is an effective refractive index. On the contrary, the reflectivity spectra of the doped QWs sample exhibit two absorption dips, on each side of the bare cavity absorption, as highlighted in the inset of Fig. 2. We fit the datasets with single and double Lorentzian absorption lines and report the extracted peak frequencies as a function of patch size s in Fig. 2(b) (open symbols). The two absorption dips in the doped QWs sample exhibit an anti-crossing behavior, characteristic of the strong light-matter coupling regime. The low (resp. high) frequency branch corresponds to the lower (resp. upper) polariton. The dispersion relation of the cavity is fitted (purple solid line) according to eq. (3), providing an effective index $n_{eff} = 3.5$ slightly larger than the refractive index of GaAs at these frequencies ($n_{GaAs} \approx 3.3$). This stems from the strong confinement of the electric field between the two metallic plates, together with field leakage and reflection phase at the edges of the cavity. The dispersion relation of the polariton branches is fitted using the secular equation[30]:

$$\left(\omega^2 - \omega_{isb}^2\right)\left(\omega^2 - \omega_c^2\right) = 4\Omega_R^2\omega_c^2 \tag{4}$$

where ω_{isb} is the intersubband transition frequency and ω_c is the cavity frequency. In the limit of very low excitation, we can safely replace the population difference by the total doping density $\Delta n = n_s$ in the expression of the Rabi frequency.

The slight discrepancy between the secular equation (4) and the data can have several causes. For instance, differences in the fabrication of the two samples might result in actual patch sizes s slightly different between the two samples from the nominal value. To correct for this effect, we assign the cavities sizes by comparing the frequency of their higher order modes (unperturbed by the ISB transition) and ensure that they match. From the fit we can extract a Rabi splitting of $2\Omega_R = 70$ cm^{-1}, which is slightly below the minimal splitting of 78 cm^{-1} measured in the $s = 1.35$ µm cavity case. These values have to be compared with the resonance frequency and the cavity/ISB transition linewidths (resp. γ_c^{tot} and γ_{isb}^{tot}), which give $\frac{\Omega_R}{\omega_{isb}} = 0.04$ and $\frac{2\Omega_R}{\gamma_{c,isb}^{tot}} = 0.65$. The Rabi frequency is comparable to the transition frequency, but the Rabi splitting is lower than the dissipation rates of the system. Since we can still resolve the polariton splitting, the system is *de facto* at the onset of the strong light-matter coupling regime.

We now measure the non-linear reflectivity of the doped QWs array closest to resonance ($s = 1.35$ µm) as a function of excitation intensity. The reflectivity is probed with a microscope setup using a commercial tunable QCL (Daylight MIRCAT) as a source and a liquid-nitrogen cooled mercury cadmium telluride detector[15].

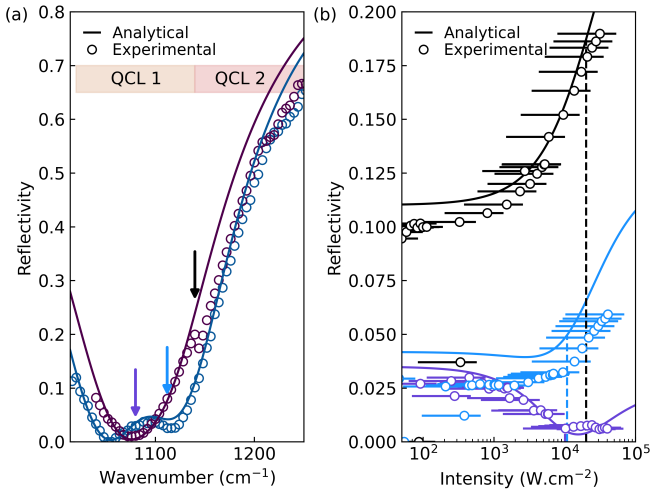

FIG. 3. (a) Reflectivity spectra of the doped $s = 1.35$ µm cavity array under low power excitation (purple circles) and high power excitation (blue circles). The solid lines are the analytical responses predicted by coupled mode theory. The two shaded area indicate the tuning ranges of the QCL chips. (b) Nonlinear reflectivity of the array as a function of the intensity for three different wavelengths indicated by the arrows in (a). Open symbols correspond to experimental data, and solid lines to the CMT prediction. The vertical dashed lines indicate the saturation condition. The horizontal error bars correspond to uncertainty on the evaluation of the spot size.

The QCL emission is amplitude modulated at 10 kHz with pulse widths of 500 ns, and lock-in detection is employed. The incident intensity can be modulated through a half-wave plate and a polarizer, and with the laser injection current. The reflectivity of the patch cavity array is normalized to that of a smooth Au surface. Fig. 3(a) reports the reflectivity spectra of the sample at very low power (blue symbols) as well as at the maximum intensity available from the QCL (purple symbols). In the low-intensity configuration, we retrieve the two absorption dip as shown in the inset of Fig. 2(a) with two polariton states. On the contrary, the high power spectrum displays only one absorption dip, centered in between the two polariton states.

We then select three distinct frequencies from the experimental spectrum in Fig. 3(a): The cavity central frequency (1080 cm^{-1}, purple arrow), the upper polariton frequency (1112 cm^{-1}, light blue arrow) and the frequency at which the reflectivity change between the two curves is the largest (1140 cm^{-1}, black arrow). Note that this frequency lies accidentally at the crossover between two QCL chips which is responsible for the small jump in the high power reflectivity spectrum. For these three frequencies we continuously scan the exciting power by rotating the halfwave plate, as well as increasing the QCL driving current. The value of the exciting power (in mW) is measured using a thermoelectric detector, and the spot size (20 µm radius at 1/e^2) is determined with a knife-edge measurement to infer the excitation intensity (in

W.cm^{-2}). The results are presented in Fig. 3(b) (open symbols). Pumping within the polariton gap at the cavity frequency leads to a decrease in reflectivity as the transition saturates, and the response of the system converges to the one of the bare cavity. On the contrary, pumping at the upper polariton frequency or on the high frequency edge of the spectrum leads to a gradual increase in reflectivity.

To get a deeper physical insight in the physics at play and describe our experiment, we use temporal coupled mode theory (CMT). The goal is to obtain an analytical expression relating the sample reflectivity (and the population difference Δn) to the incident laser intensity. The ISB transition and the cavity mode are modeled as oscillators with characteristic parameters $(\omega_i, \gamma_i, \Gamma_i)$ representing respectively their natural oscillation frequency, non-radiative, and radiative dampings. In the present case, the direct radiative coupling of the ISB transition to free-space radiation ($\Gamma_{isb} = 0$) can be neglected[31,32].

We can thus derive the equations for the evolution of the amplitude a_i of each oscillator, as well as the in- and out-coupling equation of the exciting field s^+ and s^-. This yields a set of three equations as developed in Ref.[28]:

$$\frac{\mathrm{d}a_{isb}}{\mathrm{d}t} = (i\omega_{isb} - \gamma_{isb})a_{isb} + i\Omega_R a_c \tag{5}$$

$$\frac{\mathrm{d}a_c}{\mathrm{d}t} = (i\omega_c - \gamma_{nr} - \Gamma_r)a_c + i\Omega_R a_{isb} + \sqrt{2\Gamma_r}s^+ \tag{6}$$

$$s^- = -s^+ + \sqrt{2\Gamma_r}a_c \tag{7}$$

that can be solved in the harmonic regime ($s^+ = e^{i\omega t}$) to express analytically two important quantities: the absorption $\mathcal{A}_{isb} = 2\gamma_{isb}\left|\frac{a_{isb}}{s^+}\right|^2$ solely due to the ISB transition, and the reflectivity $R = \left|\frac{s^-}{s^+}\right|^2$. Assuming (without loss of generality) that the cavity is at resonance with the ISB transition, *i.e.* $\omega_c = \omega_{isb} = \omega_0$, we have:

$$\mathcal{A}_{isb}(\Delta n) = \frac{4\gamma_{isb}\Gamma_r\Omega_R^2}{\left[(\omega-\omega_0)^2 - \Omega_R^2 - \gamma_{isb}(\gamma_{nr}+\Gamma_r)\right]^2 + \left[(\gamma_{nr}+\Gamma_r+\gamma_{isb})(\omega-\omega_0)\right]^2} \tag{8}$$

$$R(\Delta n) = \frac{\left[(\omega-\omega_0)^2 - \Omega_R^2 + \gamma_{isb}(\Gamma_r-\gamma_{nr})\right]^2 + \left[(\Gamma_r-\gamma_{nr}-\gamma_{isb})(\omega-\omega_0)\right]^2}{\left[(\omega-\omega_0)^2 - \Omega_R^2 - \gamma_{isb}(\gamma_{nr}+\Gamma_r)\right]^2 + \left[(\gamma_{nr}+\Gamma_r+\gamma_{isb})(\omega-\omega_0)\right]^2} \tag{9}$$

These expressions directly depend on the population difference Δn through the Rabi frequency (1). We then link the excited state excited population of the ISB transition n_2 in steady-state condition under an incident intensity I using the following relation:

$$n_2 = \frac{I}{N_{qw}\hbar\omega}\tau_{12}\mathcal{A}_{isb}(\Delta n) \tag{10}$$

where τ_{12} is the upper state lifetime (of the order of the ps) and N_{qw} is the number of QWs. Inserting eq. (8) in eq. (10) leads - after inversion - to the following intensity-dependent excited state population[33]:

$$I = \frac{\hbar\omega N_{qw}}{4\tau_{12}} \frac{n_2\left[\left[\gamma_{isb}(\gamma_{nr}+\Gamma_r) - \left((\omega-\omega_0)^2 - a(n_s-2n_2)\right)\right]^2 + (\omega-\omega_0)^2(\gamma_{isb}+\gamma_{nr}+\Gamma_r)^2\right]}{\gamma_{isb}\Gamma_r a(n_s-2n_2)} \tag{11}$$

where the coefficient a has been defined in eq. (1). Finally, using (9), this result allows us to establish the correspondence between the incident intensity and the measured reflectivity through the excited state population. Importantly, it allows to compute the non-linear variation of the reflectivity as a function of the pump intensity for arbitrary pumping frequencies.

Using this theory, all the experimental results (reflectivity spectra and non-linear reflectivity curves) are fitted by combining eq. (9) and eq. (11) and using a single set of parameters. The results are presented as solid lines in Fig. 3. The only free parameters are the ratio between the radiative and non-radiative cavity dissipation rates, and the ISB linewidth γ_{isb}. In fact, we fix the total quality factor $Q_c^{tot} = \frac{\omega_c}{\Gamma_r+\gamma_{nr}} = 6$ based on the total cavity linewidth $\Gamma_r + \gamma_{nr}$ measured on the undoped QW sample (Fig. 2(a)). We also fix the actual doping to $n_s = 2\cdot10^{11}\mathrm{cm}^{-2}$, as we infer it from the experimental value of the Rabi frequency using eq. (1). The fit yields $Q_r = 9.5$ and $Q_{nr} = 13$, and $Q_{isb} = 13$, and the analytical results are presented in solid lines in Fig. 3.

They quantitatively reproduce the experimental data: the collapse of the polariton states from the low intensity to the high intensity reflectivity spectra, the decrease of

the non-linear reflectivity as a function of intensity when pumping in the gap, and the increase of the non-linear reflectivity when pumping at the polariton frequency or on the high frequency edge. From the model, and particularly from eq. (11), we can further deduce the excited state population from the non-linear reflectivity curves. This allows us to mark the saturation condition (2), shown in vertical dashed lines in Fig. 3(b). Depending on the pump frequency, saturation is achieved for intensities of 10 kW.cm^{-2} to 20 kW.cm^{-2}.

We now examine the limitations of the model and its agreement to experimental data. A first approximation is made when considering that the ISB transition frequency does not depend on the saturation of the transition. In reality collective effects in confined electron gas renormalize the transition energy through the depolarization shift, according to the following formula:

$$\omega_{isb}^2(\Delta n) = \omega_{isb,0}^2 + \frac{e^2}{4\varepsilon\varepsilon_0 m^* L_{qw}}\Delta n \qquad (12)$$

where the last operand on the right-hand-side is known as the plasma frequency. In mid-IR delta-doped QWs and with such moderates doping this depolarization shift is small[34]. As we have shown, this approximation still allows to quantitatively explain our results and to readily express all results analytically in a compact form.

On the experimental side, we identify two main limitations. The first one is the non-homogeneous excitation of the patch cavity array by the (Gaussian) laser beam: all the cavities probed by the beam are actually experiencing different levels of excitation and thus exhibit different reflectivity spectra, possibly resulting in a broadening of the response. The second limitation is the precise determination of the pump spot size. Since we operate close to the maximum output power of the QCL, a strong focusing is needed to obtain high enough intensities. Even performed with great care, knife-edge measurements of the focal spot size are difficult and can lead to variations in the intensity inferred from the power measurement, as shown by the error bars in Fig. 3(b).

In conclusion, we have demonstrated absorption saturation of an ISB transition at a record low intensity (10-20 kW.cm^{-2}) by a judicious engineering of the light-matter coupling, making it compatible with mid-IR semiconductor lasers. The measured non-linear reflectivity properties have validated the analytical model of saturation in weak and strong-coupling regime that we had developed in Ref.[28]. To further improve this system, with the long-term goal of developing true semiconductor saturable absorber mirrors (SESAM) for the whole mid-IR range of the spectrum, future work will focus on improving the main figures of merit of the device: saturation intensity, reflectivity contrast, and non-saturable losses. Given the fast decoherence times of the order of hundreds of fs[35] as confirmed in recent demonstration of final state stimulation of ISB polaritons[36], and the fast population relaxation times of the order of a few ps[22,24,25,37,38] of ISB transitions, we expect fast saturation and recovery dynamics on the order of few ps[39]. Consequently, time resolved measurements using fs-pulses from optical parametric oscillators are the obvious next step. We conclude by emphasizing that this approach is in principle intrinsically scalable to the full mid-IR range. ISB transitions in III-V semiconductors are well mastered, and can cover the entire mid-infrared. And the cavity electrodynamics concepts enabling the observed ultra-low power saturation are also fully scalable to other wavelengths. We therefore believe that this experimental demonstration represents the first step towards a robust technology for mid-infrared SESAMs.

ACKNOWLEDGMENTS

This work was partially supported by the European Union Future and Emerging Technologies (FET) Grant No. 737017 (MIR-BOSE), by the French RENATECH network, and by the French National Research Agency: project SOLID (ANR-19-CE24-0003) and IRENA (ANR-17-CE24-0016). M.M. acknowledges support from the Marie Skłodowska Curie Action, Grant Agreement No. 748071. We acknowledge the technical help of the C2N cleanroom staff. We thank Iacopo Carusotto, Ammar Hideur and Adel Bousseksou for scientific discussions, Cristiano Ciuti for granting us access to the Laboratoire Matériaux et Phénomènes Quantiques cleanroom (CNRS UMR 7162, Université Paris-Cité), and Pascal Filloux for assistance in the ICP-RIE etching of the structures.

REFERENCES

[1] U. Keller, D. A. B. Miller, G. D. Boyd, T. H. Chiu, J. F. Ferguson, and M. T. Asom, "Solid-state low-loss intracavity saturable absorber for Nd:YLF lasers: An antiresonant semiconductor Fabry–Perot saturable absorber," Optics Letters **17**, 505 (1992).

[2] U. Keller, K. Weingarten, F. Kartner, D. Kopf, B. Braun, I. Jung, R. Fluck, C. Honninger, N. Matuschek, and J. Aus der Au, "Semiconductor saturable absorber mirrors (sesam's) for femtosecond to nanosecond pulse generation in solid-state lasers," IEEE Journal of Selected Topics in Quantum Electronics **2**, 435–453 (1996).

[3] U. Keller, "Recent developments in compact ultrafast lasers," Nature **424**, 831–838 (2003).

[4] Z. Qin, X. Chai, G. Xie, Z. Xu, Y. Zhou, Q. Wu, J. Li, Z. Wang, Y. Weng, T. Hai, P. Yuan, J. Ma, J. Chen, and L. Qian, "Semiconductor saturable absorber mirror in the 3-5 μ m mid-infrared region," Optics Letters **47**, 890 (2022).

[5] Q. Bao, H. Zhang, Y. Wang, Z. Ni, Y. Yan, Z. X. Shen, K. P. Loh, and D. Y. Tang, "Atomic-layer graphene as a saturable absorber for ultrafast pulsed lasers," Advanced Functional Materials **19**, 3077–3083 (2009).

[6] Y. Tan, X. Liu, Z. He, Y. Liu, M. Zhao, H. Zhang, and F. Chen, "Tuning of interlayer coupling in large-area graphene/wse2 van der waals heterostructure via ion irradiation: Optical evidences and photonic applications," ACS Photonics **4**, 1531–1538 (2017), https://doi.org/10.1021/acsphotonics.7b00296.

[7] G. Liang, X. Yu, X. Hu, B. Qiang, C. Wang, and Q. J. Wang, "Mid-infrared photonics and optoelectronics in 2d materials," Materials Today **51**, 294–316 (2021).

[8] A. Baranov and E. Tournié, *Semiconductor Lasers: Fundamentals and Applications* (Elsevier, 2013).

[9] J. Faist, *Quantum Cascade Lasers* (Oxford University Press, Oxford, 2018).

[10] H. Schneider and H. C. Liu, *Quantum Well Infrared Photodetectors: Physics and Applications*, Springer Series in Optical Sciences No. 126 (Springer, Berlin ; New York, 2007).

[11] M. Hakl, Q. Lin, S. Lepillet, M. Billet, J.-F. Lampin, S. Pirotta, R. Colombelli, W. Wan, J. C. Cao, H. Li, E. Peytavit, and S. Barbieri, "Ultrafast Quantum-Well Photodetectors Operating at 10 Mm with a Flat Frequency Response up to 70 GHz at Room Temperature," ACS Photonics **8**, 464–471 (2021).

[12] J. Hillbrand, L. M. Krüger, S. D. Cin, H. Knötig, J. Heidrich, A. M. Andrews, G. Strasser, U. Keller, and B. Schwarz, "High-speed quantum cascade detector characterized with a mid-infrared femtosecond oscillator," Opt. Express **29**, 5774–5781 (2021).

[13] M. Lagrée, M. Jeannin, G. Quinchard, O. Ouznali, A. Evirgen, V. Trinité, R. Colombelli, and A. Delga, "Direct Polariton-To-Electron Tunneling in Quantum Cascade Detectors Operating in the Strong Light-Matter Coupling Regime," Physical Review Applied **17**, 044021 (2022).

[14] G. Quinchard, C. Mismer, M. Hakl, J. Pereira, Q. Lin, S. Lepillet, V. Trinité, A. Evirgen, E. Peytavit, J. L. Reverchon, J. F. Lampin, S. Barbieri, and A. Delga, "High speed, antenna-enhanced 10.3 μ m quantum cascade detector," Applied Physics Letters **120**, 091108 (2022).

[15] S. Pirotta, N.-L. Tran, A. Jollivet, G. Biasiol, P. Crozat, J.-M. Manceau, A. Bousseksou, and R. Colombelli, "Fast amplitude modulation up to 1.5 GHz of mid-IR free-space beams at room-temperature," Nature Communications **12**, 799 (2021).

[16] H. Dely, T. Bonazzi, O. Spitz, E. Rodriguez, D. Gacemi, Y. Todorov, K. Pantzas, G. Beaudoin, I. Sagnes, L. Li, A. G. Davies, E. H. Linfield, F. Grillot, A. Vasanelli, and C. Sirtori, "10 Gbit s $^{-1}$ Free Space Data Transmission at 9 Mm Wavelength With Unipolar Quantum Optoelectronics," Laser & Photonics Reviews , 2100414 (2021).

[17] M. M. Fejer, S. J. B. Yoo, R. L. Byer, A. Harwit, and J. S. HarrisJr., "Observation of extremely large quadratic susceptibility at 9.6 – 10.8 μ m in electric-field-biased AlGaAs quantum wells," Physical Review Letters **62**, 1041–1044 (1989).

[18] P. Boucaud, F. H. Julien, D. D. Yang, J.-M. Lourtioz, E. Rosencher, P. Bois, and J. Nagle, "Detailed analysis of second-harmonic generation near 10.6 Mm in GaAs/AlGaAs asymmetric quantum wells," Applied Physics Letters **57**, 215–217 (1990).

[19] E. Rosencher, A. Fiore, B. Vinter, V. Berger, P. Bois, and J. Nagle, "Quantum Engineering of Optical Nonlinearities," Science **271**, 168–173 (1996).

[20] J. Lee, M. Tymchenko, C. Argyropoulos, P.-Y. Chen, F. Lu, F. Demmerle, G. Boehm, M.-C. Amann, A. Alù, and M. A. Belkin, "Giant nonlinear response from plasmonic metasurfaces coupled to intersubband transitions," Nature **511**, 65–69 (2014).

[21] J. Yu, S. Park, I. Hwang, D. Kim, J.-Y. Jung, and J. Lee, "Third-Harmonic Generation from Plasmonic Metasurfaces Coupled to Intersubband Transitions," Advanced Optical Materials **7**, 1801510 (2019).

[22] A. Seilmeier, H.-J. Hübner, G. Abstreiter, G. Weimann, and W. Schlapp, "Intersubband relaxation in GaAs- Al x Ga 1 - x As quantum well structures observed directly by an infrared bleaching technique," Physical Review Letters **59**, 1345–1348 (1987).

[23] F. H. Julien, J.-M. Lourtioz, N. Herschkorn, D. Delacourt, J. P. Pocholle, M. Papuchon, R. Planel, and G. Le Roux, "Optical saturation of intersubband absorption in GaAs-Al $_x$ Ga $_{1-x}$ As quantum wells," Applied Physics Letters **53**, 116–118 (1988).

[24] K. L. Vodopyanov, V. Chazapis, C. C. Phillips, B. Sung, and J. S. Harris, "Intersubband absorption saturation study of narrow III - V multiple quantum wells in the spectral range," Semiconductor Science and Technology **12**, 708–714 (1997).

[25] S. A. Mann, N. Nookala, S. C. Johnson, M. Cotrufo, A. Mekawy, J. F. Klem, I. Brener, M. B. Raschke, A. Alù, and M. A. Belkin, "Ultrafast optical switching and power limiting in intersubband polaritonic metasurfaces," Optica **8**, 606 (2021).

[26] R. I. Woodward, M. R. Majewski, and S. D. Jackson, "Mode-locked dysprosium fiber laser: picosecond pulse generation from 2.97 to 3.30 µm," APL Photonics **3**, 116106 (2018).

[27] M. R. Majewski, R. I. Woodward, J.-Y. Carreé, S. Poulain, M. Poulain, and S. D. Jackson, "Emission beyond 4 micron and mid-infrared lasing in a dysprosium-doped indium fluoride (inf3) fiber," Opt. Lett. **43**, 1926–1929 (2018).

[28] M. Jeannin, J.-M. Manceau, and R. Colombelli, "Unified Description of Saturation and Bistability of Intersubband Transitions in the Weak and Strong Light-Matter Coupling Regimes," Physical Review Letters **127**, 187401 (2021).

[29] J.-M. Manceau, N.-L. Tran, G. Biasiol, T. Laurent, I. Sagnes, G. Beaudoin, S. De Liberato, I. Carusotto, and R. Colombelli, "Resonant intersubband polariton-lo phonon scattering in an optically pumped polaritonic device," Applied Physics Letters **112**, 191106 (2018).

[30] Y. Todorov, A. M. Andrews, R. Colombelli, S. De Liberato, C. Ciuti, P. Klang, G. Strasser, and C. Sirtori, "Ultrastrong Light-Matter Coupling Regime with Polariton Dots," Physical Review Letters **105**, 196402 (2010).

[31] F. Alpeggiani and L. C. Andreani, "Semiclassical theory of multisubband plasmons: Nonlocal electrodynamics and radiative effects," Physical Review B **90** (2014), 10.1103/PhysRevB.90.115311.

[32] M. Jeannin, T. Bonazzi, D. Gacemi, A. Vasanelli, L. Li, A. G. Davies, E. Linfield, C. Sirtori, and Y. Todorov, "Absorption Engineering in an Ultrasubwavelength Quantum System," Nano Letters **20**, 4430–4436 (2020).

[33] A. Baas, J. P. Karr, H. Eleuch, and E. Giacobino, "Optical bistability in semiconductor microcavities," Physical Review A **69**, 023809 (2004).

[34] R. Cominotti, H. A. M. Leymann, J. Nespolo, J.-M. Manceau, M. Jeannin, R. Colombelli, and I. Carusotto, "Theory of coherent optical nonlinearities of intersubband transitions in semiconductor quantum wells," arXiv 2109.00285 (2021).

[35] R. A. Kaindl, K. Reimann, M. Woerner, T. Elsaesser, R. Hey, and K. H. Ploog, "Homogeneous broadening and excitation-induced dephasing of intersubband transitions in a quasi-two-dimensional electron gas," Physical Review B **63**, 161308 (2001).

[36] M. Knorr, J. M. Manceau, J. Mornhinweg, J. Nespolo, G. Biasiol, N. L. Tran, M. Malerba, P. Goulain, X. Lafosse, M. Jeannin, M. Stefinger, I. Carusotto, C. Lange, R. Colombelli, and R. Huber, "Intersubband Polariton-Polariton Scattering in a Dispersive Microcavity," Physical Review Letters **128**, 247401 (2022).

[37] S. Lutgen, R. A. Kaindl, M. Woerner, T. Elsaesser, A. Hase, and H. Künzel, "Nonlinear intersubband absorption of a hot quasi-two-dimensional electron plasma studied by femtosecond infrared spectroscopy," Physical Review B **54**, R17343–R17346 (1996).

[38] S. Lutgen, R. A. Kaindl, M. Woerner, T. Elsaesser, A. Hase, H. Künzel, M. Gulia, D. Meglio, and P. Lugli, "Nonequilibrium Dynamics in a Quasi-Two-Dimensional Electron Plasma after Ultrafast Intersubband Excitation," Physical Review Letters **77**, 3657–3660 (1996).

[39] J. Raab, C. Lange, J. L. Boland, I. Laepple, M. Furthmeier, E. Dardanis, N. Dessmann, L. Li, E. H. Linfield, A. G. Davies, M. S. Vitiello, and R. Huber, "Ultrafast two-dimensional field spectroscopy of terahertz intersubband saturable absorbers," Optics Express **27**, 2248 (2019).